



Time and path prediction of landslides using InSAR and flow model

Priyom Roy^{*}, Tapas R. Martha, Kirti Khanna, Nirmala Jain, K. Vinod Kumar

Geodynamics and Geohazards Division, Geosciences Group, National Remote Sensing Centre (NRSC), Indian Space Research Organisation (ISRO), Hyderabad 500 037, India

ARTICLE INFO

Editor: Jing M. Chen

Keywords:

Debris flow
Accelerating landslide
PSI
SBAS
Displacement

ABSTRACT

Landslides originating from remote steep slopes render people living downhill vulnerable, unaware of the impending danger. Identifications of slow-moving mountain slopes are possible now due to time series measurement from space using microwave satellite data and the InSAR technique, which potentially can detect displacement at millimetre level. Availability of open-source Sentinel-1 data has revolutionised the study involving landslide kinematics and predicting the time of failure. However, identification of accelerating trend, demarcation of release area and prediction of flow path after failure initiation are still challenging. In this paper, we present a novel method for time and path prediction of landslides using two large landslides (Kikruma and Kotropi) located in the Himalayas in India. Sentinel-1 data stack was processed using the Persistent Scatterer and Small Baseline Subset interferometric techniques to analyse the trend of ground deformation leading to slope failures. The displacement time series of the measurement points, analysed using inverse velocity and modified inverse velocity methods, show that the instability had commenced almost a year or more with the final onset of acceleration triggered by heavy rainfall, couple of weeks prior to the actual failure. The acceleration image created from displacement time series data was clustered using image segmentation techniques to demarcate the release area of landslides. The flow simulation was done using the Voellmy friction model with a high-resolution DEM to predict the flow path. The analysis done for Kikruma and Kotropi landslide case studies with the proposed method provided a safe prediction of the time of landslide with ~90% accuracy of the flow path prediction. Results show that the method demonstrated in this study may evolve as an effective tool for landslide early warning in hilly areas.

1. Introduction

Landslides are among the main natural catastrophes, which cause major problems in mountainous terrain by killing hundreds of people every year besides damaging property, blocking transportation and disrupting communication links. In some areas, such as the western coastal parts of North and South America, Central America, Alpine regions of Italy, France, Switzerland and Austria in Europe, Himalayan regions of India and Nepal in Asia and parts of Central Asia, the effects of landslides are more pronounced mainly due to spurred developmental activities to meet the ever-growing demand of people (Petley, 2013). As per the official figures, between 1998 and 2017, landslides have caused more than 18,000 deaths worldwide¹. A recent study by Froude and Petley (2018) on global fatal landslides showed that the spatial distribution of landslides is heterogeneous, with Asia representing the dominant (75%) geographical area. As per this study that collated a non-

seismic landslide database, India ranks first among all nations in the world in terms of number of fatal landslides. Hence, there is an urgent need to formulate strategies for minimising the impact of landslides. Prediction of the occurrence of landslide event in time and space remains a challenge owing to the inherent landslide process complexities. However, with advanced remote sensing measurements coupled with numerical simulation, broad predictions about the day of occurrence and path or propagation of material with its important behavioural parameters could be estimated which can assist damage assessment (Bekaert et al., 2020; Zhang et al., 2012; Strozzi et al., 2005; Dong et al., 2018; Hu et al., 2020a, 2020b; Mondini et al., 2021).

Differential InSAR is a proven technique for measuring surface deformation induced by various geophysical phenomena such as earthquakes, volcanoes, landslides and over-exploited aquifers (Carnec et al., 1996; Rott et al., 1999; Raspini et al., 2018; Amelung et al., 2000; Bürgmann et al., 2000; Strozzi et al., 2005; Motagh et al., 2008).

^{*} Corresponding author.

E-mail address: roy.priyom@gmail.com (P. Roy).

¹ Worldwide landslide death statistics: www.who.int (accessed on 11 March, 2021).

However, InSAR is limited by temporal and geometrical decorrelations (Zebker and Villasenor, 1992) and atmospheric delay anomalies (Massonnet and Feigl, 1998). In the last 20 years, multi-temporal InSAR technologies (e.g. Persistent Scatterer Interferometry (PSI), Small Baseline Subset (SBAS)) were developed to overcome such limitations by using large number of SAR images for computing displacement time series (Ferretti et al., 2001; Bernardino et al., 2002). PSI and SBAS have acquired wide popularity in the last decade in terms of deformation monitoring (Bernardino et al., 2002; Ferretti et al., 2001; Kampes and Hanssen, 2004; Casu et al., 2006; Prati et al., 2010). These techniques process radar images acquired over the same area, but at a different time period, and measure deformation through interferometric methods (Singh Roy et al., 1998; Ferretti et al., 2007). The number of SAR images should be large and coherent with one another to monitor displacements accurately within the time period. These methods when applied on a hill slope areas can indicate movement over time which may eventually lead to a failure. Therefore, PSI and SBAS methods are extensively used in landslide studies, such as landslide investigation and identification (Yin et al., 2010; Del Soldato et al., 2018; Boni et al., 2018), landslide inventory mapping and activity assessment (Righini et al., 2012; Cigna et al., 2013), slow landslide displacement monitoring, mapping of landslide areas and understanding landslide kinematics (Herrera et al., 2011; Zhao et al., 2018; Lu et al., 2012; García-Davalillo et al., 2014; Schlögel et al., 2015; Rosi et al., 2018).

The velocity time series of slope movement can be directly used to predict the time of failure of the slope (Intrieri et al., 2017). The time of failure (t_f) can be predicted using mathematical formulations of which the most widely used in the domain of landslide prediction is the Inverse Velocity (INV) method (Fukuzono, 1985a&b). As per the creep theory, an ideal landslide deformation-time curve shows three stages of deformation i.e. primary, secondary and tertiary, correlating to an initial slow deformation stage, an intermittent steady deformation stage and a final accelerated deformation stage, respectively (Crosta and Agliardi, 2003; Saito, 1996). The INV method predicts the landslide failure time by linearly fitting the distribution of the inverse velocity estimates in the third stage of a creep. The INV method was further modified by Zhou et al. (2020) as the Modified Inverse Velocity (MIV) method to enhance the accuracy of prediction of t_f , by extending the formulation of the earlier method. However, the precise application of these methods involves accurate and reasoned identification of representative locations on the landslide body (through PSI and SBAS), which shows the clear onset of the tertiary stage of deformation (acceleration).

In addition to the time prediction of failure, it is also necessary to model the runout of the landslide in space, so as to understand the extent of the flow and the consequent affected area. Runout modelling mainly depends upon the characteristics of release area and runout path, type of triggering process and lastly on the type and volume of material deposited (Luna et al., 2013). Runout prediction models can be empirical, statistical, physical or dynamically based, depending on the available input (Schraml et al., 2015). Empirical-Statistical based approaches were developed to model runout path using flow volume (Guthrie and Befus, 2021; Tang et al., 2012) and require limited ground information while physically based dynamic model mostly depends upon fluid mechanics equations and significant amount of ground information. The Rapid Mass Movement Simulation (RAMMS ©) which is based on a 2-D Voellmy-fluid friction model has found wide applications in the simulation of mass movements, especially snow avalanches, rockfall and debris flow (Kumar et al., 2018; Bovis and Jakob, 1999). The model takes single or multiple blocks as release area (initiation) and uses two parameters of Voellmy relation to describe the frictional behaviour of the flow (Mergili et al., 2017; Berger, 2010; Berger et al., 2011; Rickennann, 1999). Defining an accurate release area for a hill slope debris flow is a challenging aspect of the model as it provides useful information about the total volume, flow velocity, flow height and total pressure.

In this study, we demonstrate a novel method for time and path

prediction of landslides using PSI, SBAS and numerical simulation of debris flows using RAMMS. We showcase the results for the Kikruma and Kortropi landslides which occurred in the state of Nagaland and Himachal Pradesh, respectively, in India. We decipher the motion of slope material from the PSI and SBAS derived displacement time series and identify areas of instability from the measurement points (MP). We use the velocity-time series to estimate the time of failure using INV and MIV methods (Fukuzono, 1985a, 1985b; Zhou et al., 2020). We further demonstrate the constraints of each method, especially when used in tandem with PSI and SBAS. Further, from the accelerating MP image, we demarcate the release area using an image segmentation method. The release area is used to model the runout extent of the flow using RAMMS. The results are then compared with the actual ground scenario to demonstrate the applicability of the method.

2. Study areas

The Himalayas extending across the Indian subcontinent host a diverse suite of rock types and structural discontinuities vulnerable to landslides (Martha et al., 2021). Therefore, the mechanism and geometry of slope failures vary from northwest to northeast of India. To create a representative workflow of landslide time and path prediction, test cases from both the north-western and north-eastern India need to be studied and demonstrated. We have therefore chosen two cases namely the Kikruma landslide from the eastern Himalaya and the Kotropi landslide from the western Himalaya in India.

2.1. Kikruma landslide

A large landslide was triggered on 29 July 2018 near Kikruma village in Phek district of Nagaland, resulting in the formation of an artificial dam on the Sidzu River causing an imminent threat to the habitations downstream (GSI, 2018). The landslide is located on the northern part of the Kikruma village².

The Kikruma landslide is located at 25°36'15.5"N latitude and 94°13'19.5"E longitude (Fig. 1a and b). The lithology around the landslide comprises highly shattered, sheared sequences of grey splintery shale, lensoidal fine-grained sandstones with greywacke and rhythmites of Upper Disang Formation³. The landslide has occurred along a west-facing slope of the N-S trending ridge. The length, width and height of the landslide are 1200 m, 600 m and 470 m, respectively. The failure mechanism is deep translational (planar).

2.2. Kotropi landslide

On 13 August 2017, a massive landslide occurred near the Kotropi village (near Kotropi bus stop) in the Mandi District of Himachal Pradesh (Fig. 1c and d). The landslide occurred on National Highway 154, between Mandi and Pathankot (Roy et al., 2018; Pradhan et al., 2019).

The Kotropi landslide is located at 31° 54' 43.6"N latitude and 76° 53' 16.4"E longitude lying within the Lesser Himalayas with an altitude variation of about 350-1500 m. Greenish Shale with Purple Mudstone belonging to the Dharamshala Group is present in the inaccessible upper part of the main body of landslide. The study area falls in a thrust contact zone (Main Boundary Thrust) between the Shali and the Lower Tertiary group of rocks such as mudstones, dolomites, purple clay, micaceous sandstones and brick red shale (Pradhan et al., 2019). The landslide is a mixed 'debris flow' type with a rotational failure mechanism near the crown. It has a long runout zone which clearly suggests that heavy rainfall is the main triggering factor. The area of the landslide is

² Kikruma landslide media report : www.morungexpress.com (accessed on 11Feb, 2021).

³ Geological map of India in 1:50000: www.bhukosh.gsi.gov.in (accessed on 10 January, 2021).

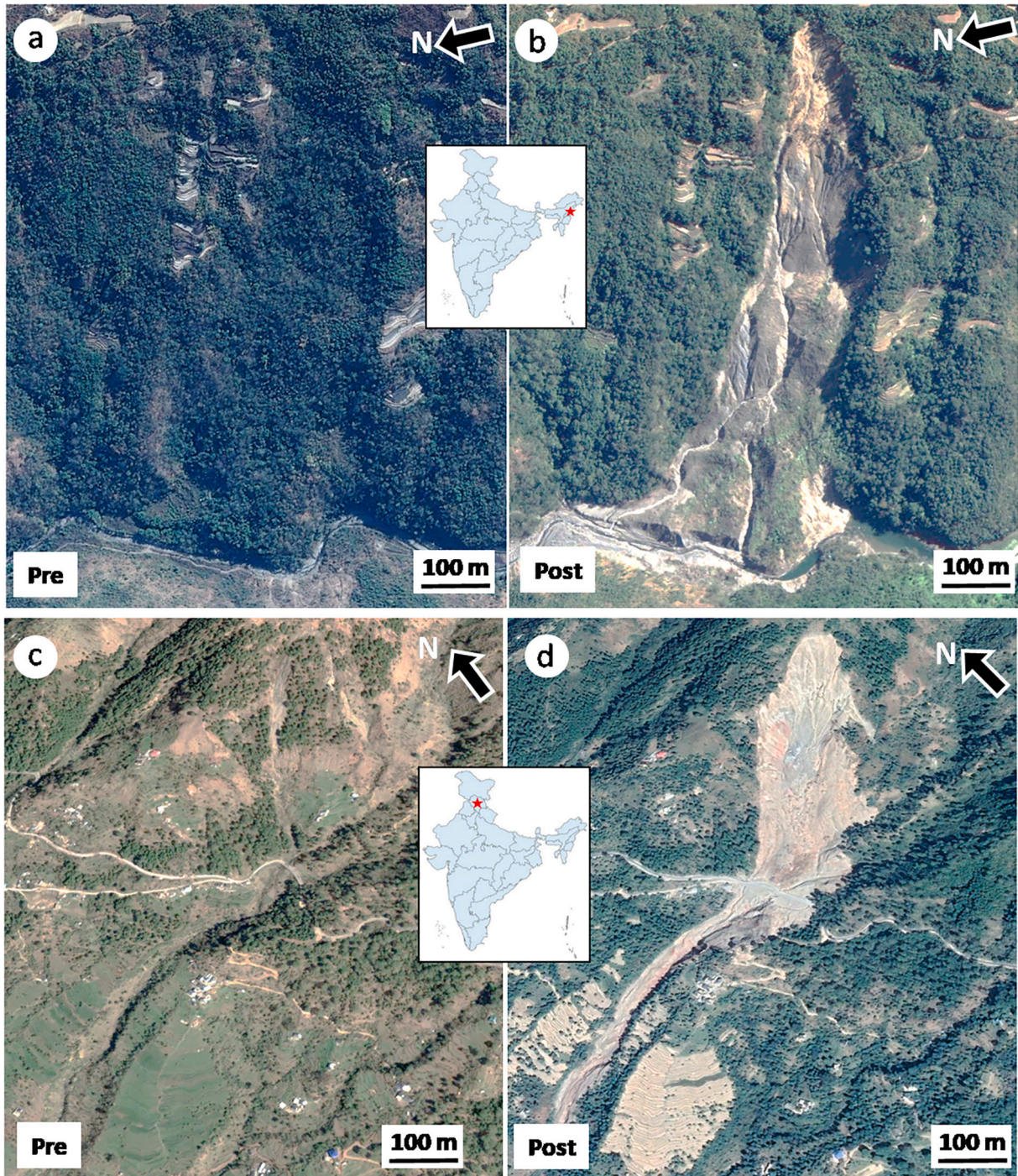


Fig. 1. a. Pre-event satellite image of Kikruma Landslide b. Post-event satellite image of Kikruma Landslide. c. Pre-event satellite image of Kotropi Landslide. d. Post-event satellite image of Kotropi Landslide. Insets show location of landslide on India map. (Source: Google Earth).

133,674 m² and the width of the landslide is 190 m and the runout length is 1155 m.

3. Material and methods

3.1. Sentinel-1 imagery

Sentinel-1 is a Synthetic Aperture Radar (SAR) mission, providing continuous all-weather, day-and-night imagery in C-band with a centre frequency of 5.4 GHz, operating in four exclusive imaging modes with different spatial resolutions and coverages⁴. Sentinel-1 has been successfully used in Earth surface deformation monitoring worldwide (Bui et al., 2021). Data products are available in single polarisation (VV or HH) for Wave mode and dual polarisation (VV + VH or HH + HV) and single polarisation (HH or VV) for Stripmap (SM), Interferometric wide (IW) and Extra wide (EW) swath modes. In IW mode, Sentinel-1A, which was launched in April 2014, can map global landmasses once every 12 days. The launch of Sentinel-1B in April 2016 enabled a two-satellite constellation that can deliver a six-day repeat cycle. Sentinel-1 interferometric products also help to ensure a high density of persistent scatterers to provide velocity (line of sight) measurements. We have selected the images from first available data till the date of failure for InSAR analysis. The available archive of Sentinel-1, including 42 images and spanning the time interval from 21 March 2017 to 26 July 2018 (three days prior to slope failure), has been processed for the Kikruma landslide. Similarly, 42 images spanning the time interval from 15 November 2015 to 12 August 2017 (one day prior to slope failure), have been processed for the Kotropi landslide. PSI and SBAS processing was carried out using SARSCAPE © software (SARMAP, 2012). Images have been captured along satellite track number 143 in ascending orbit for Kikruma and along satellite track number 136 in descending orbit for Kotropi with an incidence angle of ~30° to 40°. The Sentinel-1 datasets over the two areas of interest are available at an interval of 12 days.

3.2. Delineation of instability using PSI and SBAS

The purpose of the InSAR analysis here was to retrieve information on ground deformation, with a particular focus on the identification of possible precursory motion of the Kikruma and Kotropi landslides. We used PSI and SBAS methods to understand the ground deformation and generate the displacement time series of the MPs. We attempted both the methods and combined the result to ensure a uniform distribution of resultant MPs and cross validate the deformation trends of both the methods towards prediction of the time of failure. The PSI method is intended for the analysis of point targets. The number of acquisitions is crucial for coherence estimation, which, in turn enables the identification of a suitable number of PS. Since the image covers a 250 km swath, the subset covering the landslide was selected using the “sample selection SAR geometry tool”. This is a predefined module in the SARSCAPE environment which is used to subset the data using a user defined area of interest. Shuttle Radar Topographic Mission (30 m) global Digital Elevation Model (DEM) was used to eliminate the topographic phase. Five major steps are involved for processing Sentinel-1 data using the PSI technique through the SARSCAPE © environment. The first step is a connection graph wherein the best primary image is selected automatically by the software among all the acquisitions on the basis of the most reliable connections between them. The position and distance plots are generated for all the secondary images with respect to the primary image. After the suitable selection of the primary image, the interferometry process was applied and differential interferograms for all secondary images with respect to primary image were generated. Image to image coherence is a key criterion for appropriate PS generation and

distribution. In the case of landslide related ground displacements, slope material and vegetation cover tends to lower the coherence. Therefore, for our study we have adopted a coherence threshold of 0.60 for both study areas. Displacement, velocity and coherence will be generated from these interferograms in the first and second inversions step leading to the identification of PS. The first inversion estimates the residual height with displacement and velocity. They are used to flatten the complex interferograms. The second inversion uses a linear model to estimate the atmospheric phase components. The linear model is subtracted from all differential interferograms in order to refine the velocity and residual height values (SARMAP, 2012).

On the other hand, the SBAS technique relies on a network selection of the SAR data pairs to generate interferograms. SBAS is advantageous, as a network of redundant interferograms is used to reduce the noise in the resultant deformation time series (Bui et al., 2020). They are characterised by a small temporal and spatial separation (baseline) between the orbits in order to limit the noise effects referred to as decorrelation phenomena (Ferretti et al., 2001; Lauknes et al., 2011). The SBAS method measures deformations of a combination of distributed targets (i.e. low intensity scatterers) and dominant targets (i.e. high intensity scatterers) such as large rock faces, from the filtered and unwrapped phases (Lauknes et al., 2011). The second step of the procedure involves the retrieval of the original (unwrapped) phase signals from the modulo-2 π restricted (wrapped) phases directly computed from the interferograms. The SBAS processing chain consists of extending the analysis to those resolution cells where the information has some temporal gaps because of the signal decorrelation, leading to coherence values smaller than the acceptable threshold. Therefore, we have used a coherence threshold equal to 0.3 in our analysis. Further, the perpendicular baseline thresholds for SBAS processing is kept at 4% of the threshold of the critical baseline (Dun et al., 2021). We have provided the interferogram networks and mean coherence maps in supplementary material 1. Given that both the landslides are slow moving, a trade-off of temporal baseline was required to capture the deformation signal vis-a-vis coherence loss. Therefore, we have optimally selected 75 days as the temporal baseline threshold (SARMAP, 2012; Dun et al., 2021). We have provided the interferogram networks as supplementary material 1. In InSAR data processing, filtering can be applied in various steps to reduce the noise in interferograms (Goldstein and Werner, 1998) or in resultant deformation time series (Khaki et al., 2020). We have used Goldstein filtering algorithm during the interferogram generation to reduce phase noise as much as possible. As the study areas are mountainous and have vegetation cover, we have set the minimum and maximum filtering thresholds to 5 and 8, respectively (Dun et al., 2021).

The crucial step of the SBAS approach is the inversion of the unwrapped interferograms for the deformation time series retrieval. Further, availability of space/time information enables the detection and subsequently filtering of possible atmospheric artefacts.

The last step of the PSI and SBAS process is geocoding, in order to produce the geocoded shapefiles and/or raster files. In addition to the geocoded products, a shapefile of the MPs is generated with attribute information containing line of sight (LOS) displacement (D_{los}) for each observation date. This is used to generate the displacement time series and estimate LOS velocities (V_{los}) using a linear fit and their variation leading to failure. This is the key information required for the prediction of the time of failure using INV (Fukuzono, 1985a) and MIV (Zhou et al., 2020) methods. Herein, the time of failure refers to the day of occurrence of the landslide.

3.3. Prediction of time of failure

The time of failure estimation involves careful scrutiny and selection of candidate MPs which are to be further used in the calculation. We have used INV and MIV methods to estimate the time or window of failure from candidate MPs.

⁴ Sentinel-1 mission information: <https://sentinel.esa.int/web/sentinel/missions/sentinel-1> (accessed on 11 March, 2021).

3.3.1. Selection of candidate measurement points

Analysis of the MPs enables identification of at least three different types of kinematic behaviours which can be grouped as accelerating, linear and stable. The accelerating areas are most important for detection of slope failure as they are directly related to the signatures of slope instability. The acceleration or tertiary creep precedes the collapse, from which the time of failure can be forecasted (Saito, 1996; Fukuzono, 1985a; Rose and Hungr, 2007; Mufundirwa et al., 2010; Carlà et al., 2018). We have analysed the displacement time series curves generated from the PSI and SBAS results and have selected such accelerating MPs for further analysis. The accelerating MPs are selected from the crown and flank of the landslides to adequately represent the overall landslide kinematics. To ascertain the quality of the individual MPs, we have estimated the “relative precision (r)” where $r = (V_p/V_{10s})$. V_p can be estimated using Eq. (1) of Kovács et al. (2019). MPs with |r| value less than 100 are considered to be reliable and hence are further analysed. The displacement time series curves for these MPs clearly demarcate the tertiary phase of deformation.

3.3.2. Inverse velocity method

The INV is a graphical method described by Fukuzono (1985a). It consists of plotting the inverse of velocity against day of observation (time). The ratio of displacement by number of days of observation gives an estimate of the velocity in mm per day. A reciprocal of the velocity value yields the inverse velocity corresponding to a particular time of observation. In our case, the first day of observation is the day of available first acquisition and the consequent days are then numbered accordingly till the date of last acquisition for both the landslide instances. This implies that the entire time series of velocity information encompasses a total of 492 days for Kikrumba and 636 days for Kotropi. As long as there is equilibrium, the inverse velocity time plots a line which is parallel to time axis. When the instability is triggered, the inverse velocity decreases asymptotically and the plot display a best fit line which on extrapolation intersects the time axis. This day corresponds to the day of failure.

3.3.3. Modified inverse velocity method

The MIV method was proposed by Zhou et al. (2020) to estimate the time of failure using the velocity information derived from the PSI and SBAS processing outcomes. The estimated velocity time series is converted to inverse velocity time series with respect to the observation days (as described in section 3.3.2). We used the mathematical formulation of the MIV (Eq. (1)) to deterministically estimate the t_f using the information derived from the displacement time series graphs of individual MPs. We estimated the day of onset of acceleration (OOA) from the change in trend of the displacement-time graph (Dick et al., 2015). This day is marked as t_0 and observed as the penultimate change in trend of the displacement time series prior to failure. The inverse velocity estimated by calculating the reciprocal of the velocity value corresponding to t_0 is marked as $1/v_0$. Using these two parameters, the t_f is estimated as follows:

$$\frac{1}{v} = \frac{1}{v_0} \times \left(1 + \frac{t_0 - t}{t_f - t}\right) \quad (1)$$

The t_0 estimate from the OOA is the demarcated as the penultimate change in the trend of displacement time series prior to failure. The values of t and corresponding v are taken to be the day of last observation of the time series.

3.4. Flow modelling

The final step is to numerically simulate the failure path and run out distance. This is essential to identify the possible impact area and also to estimate probable damage scenarios. In our study, we have chosen the 2-D Voellmy-fluid friction model as implemented in RAMMS (Ayotte and

Hungr, 2000). The model aims to calculate the motion of the movement from initiation to runout in three-dimensional terrain. It uses depth-averaged equations and predicts the slope-parallel velocities and flow heights. The flow height determines the height of the debris while velocity determines the flow movement.

The main input parameters to be ingested in the flow model are DEM, release area and friction information. RAMMS is sensitive to the resolution of the DEM. Hence, we have used the high resolution CartoDEM (2.5 m) for flow modelling (Martha et al., 2010a, 2010b; Sharma and Kartikeyan, 2014). The model takes single or multiple blocks or release area (zone of initiation) or input hydrograph (if field observations are available) and use two-parameter Voellmy relations to describe the frictional behaviour of the flow. Defining an accurate release area for a hill slope debris flow is an important aspect of the model as it provides useful information about, total volume, flow velocity, flow height and total pressure.

3.4.1. Estimation of the release area

We have demarcated the release area based on the clustering of acceleration of all MPs derived from the PS and SBAS output. The acceleration of the individual MPs is estimated by subtraction of the velocity of the last observation day from the velocity of the penultimate observation day and dividing the same by time. We assume that the cluster of high acceleration points defines the general zone of instability on the slope face and thus will be the region to fail in the case of a triggering event which in this case is heavy rainfall. The PS and SBAS point dataset was converted into an acceleration image using the inverse distance weighted interpolation method. This image illustrates the variation of acceleration within the landslide zone. This image is further segmented to low, moderate and high acceleration class and the areas of high acceleration above the break-in slope of MP(s) showing OOA were considered as the release area during the slope failure. In absence of any apriori field information, the entire release area was considered as a single block of fixed depth in the RAMMS simulation environment.

To estimate the release volume, we have a generalised landslide volume-area relationship applicable to this terrain and given by Larsen et al. (2010) as described in Eq. (2).

$$V = 0.186 * A^{1.35} \quad (2)$$

Where V is the volume and A is the area of the landslide.

Once the volume is calculated, it is converted into respective block depths by dividing the volume with the RA. These block depths or depths of RAs are used for the flow simulation.

3.4.2. Flow simulation

Density, coefficients of dry coulomb (μ) and viscous turbulent (ξ) frictions are important input parameters to control the overall flow geometry (Ayotte and Hungr, 2000). The density values are adopted from the data published by Pradhan et al. (2019) for the Kotropi landslide. In both scenarios, the approach of selecting μ and ξ coefficients has been kept similar. The μ is considered constant with the value of 0.21 for Kikrumba (tangent of the average slope, e.g. for Kikrumba it is 12° at the zone of deposition). From the geological interpretations, the rock types in the region tend to be granular, therefore with fixed μ , we have iterated ξ with values of 100, 150 and 200. For the Kotropi landslide, the average slope values are 16° at the zone of deposition for which μ has been assigned with a value of 0.29. This constant value of μ is again iterated with ξ values of 100, 150 and 200, determining the range for granular type debris flow as suggested in the RAMMS debris flow manual. Using these parameters, we attempt to model the flow extent which is the best representative of the ground condition using Eq. (3) (Salm et al., 1990; Salm, 1993).

$$S = \mu N + (\rho g u^2 / \xi) \quad \text{with } N = \rho h g \cos(\varphi) \quad (3)$$

where ρ is the density, g the gravitational acceleration, φ the slope angle,

h the flow height and u the vector $u = (u_x, u_y)^T$, consisting of the flow velocity in the x- and y-directions. The normal stress, N on the running surface can be summarised as $\rho h g \cos(\phi)$. The Voellmy model accounts for the friction coefficients which are responsible for the behaviour of the flow, μ dominates when the flow is close to stopping; ξ dominates when the flow is moving fast. Once the flow is simulated, we carried out an accuracy estimation of the predicted vs. actual flow using metrics such as branching factor (Bf), miss factor (Mf) and detection percentage (Shufelt, 1999; Lee et al., 2003; Martha et al., 2012). Branching and miss factors indicate two types of potential errors, i.e. false positive and false negative areas that may be generated in the simulation process. Detection percentage indicates the landslide area correctly simulated. A combination of low Bf and high detection percentage indicates high accuracy of the simulation result.

The entire method is illustrated by the flow chart in Fig. 2.

4. Results

4.1. Displacement and velocity estimation from PSI and SBAS

The PSI algorithm applied to the Sentinel-1 data stack provided significant information on the movement of the slope material before the landslide occurrence. Though vegetation cover impaired the scene-to-scene coherence and limited the number of PS in the landslide region, we were able to achieve ~500 PS MPs for Kikruma (Fig. 3a) and ~400 PS MPs for Kotropi (Fig. 3b). Given the overall vegetation cover of the slopes, which is much denser in the case of Kikruma, the SBAS processing for Kikruma did not yield any MPs due to absence of distributed scatterers and has resulted in ~140 MPs for Kotropi (Fig. 3c).

Accurate selection of representative MPs is essential for the acceptable prediction of failure time. The location of the selected accelerating

MPs from the crown and flanks of the landslides are shown in Fig. 3. It is observed that modal values of LOS velocity representing subtle state of activity of landslides are generally in the range of 3–5 mm/y. Any velocity of more than 5 mm/y generally signifies an active deformation phase of the landslide (Crippa et al., 2021). Additionally, Kovács et al. (2019) demonstrated that in mountainous and vegetated areas, scatterers are corrupted by noise if LOS velocity is less than 6–7 mm/yr. Therefore, we have analysed the displacement time series of the all the MPs with threshold velocities of more than 5 mm/yr demarcating them as unstable. As mentioned in section 3.3.1, considering the kinematic behaviour, the MPs can be categorised as un-deformed, stable displacement and accelerating displacement in the tertiary phase of deformation (Fig. 4). MPs with linear displacement show a secondary phase of acceleration and have not attained the tertiary phase. Whereas, MPs with accelerating displacement, show a continuous increase (linear or exponential) in cumulative displacement over time in the tertiary phase (Intrieri et al., 2017). We have chosen the MPs which are showing accelerating displacement time series for further analysis. It is seen that for both the landslides, accelerating MPs are found to exhibit two distinct trends. Few MPs show continuous trends of acceleration which can be perfectly defined by a quadratic trend line. Others show more realistic naturally representative displacement patterns with intermittent phases of stability and instability (Fig. 4). We carefully select such naturally representative MP for the prediction of the time of failure.

4.2. Prediction of failure time

Using the displacement time series of the accelerating MPs, we have attempted to estimate the time of failure using the INV and MIV methods. As discussed in the previous section, the displacement time series is studied for the change in the trend of the curve. For both INV

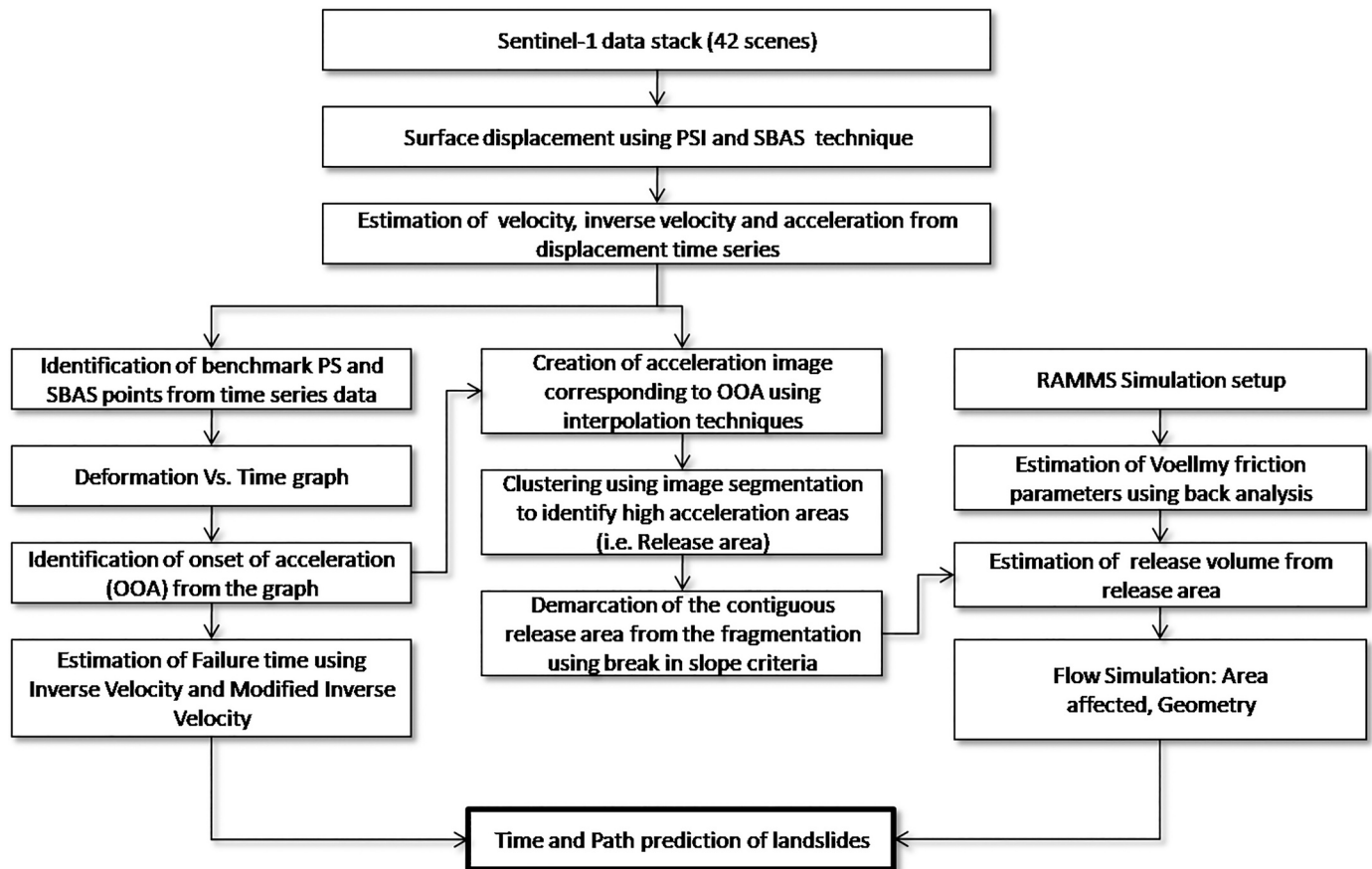


Fig. 2. Flowchart of the methodology.

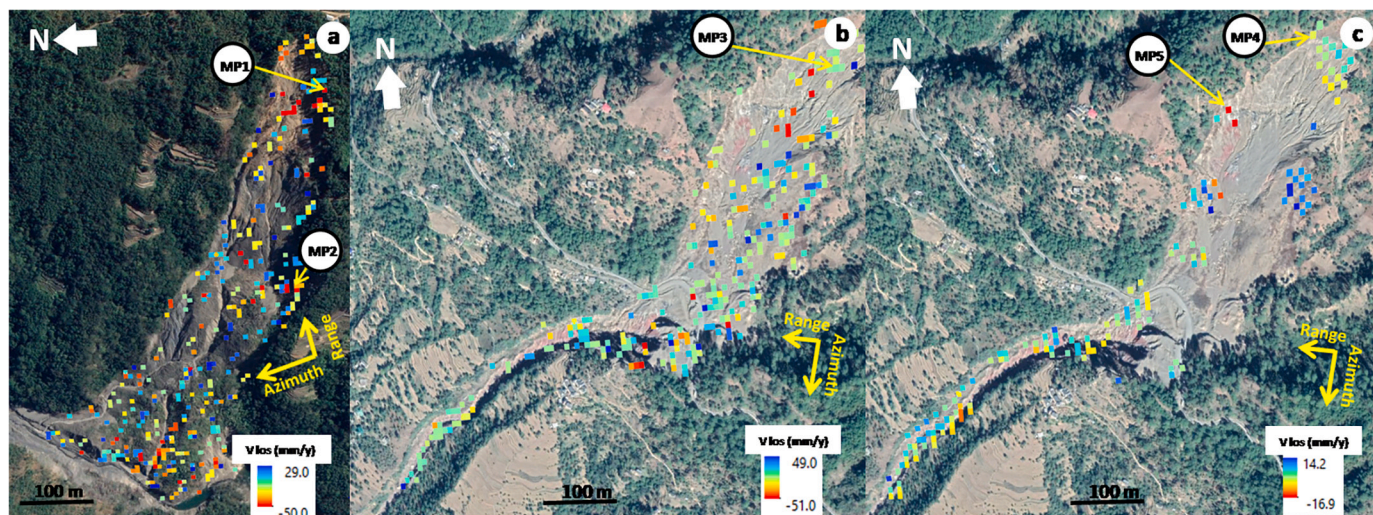


Fig. 3. a) Distribution of PS points in Kikruma; b) Distribution of PS and SBAS points in Kotropi landslide areas. Location of accelerating MPs (1–5) are annotated.

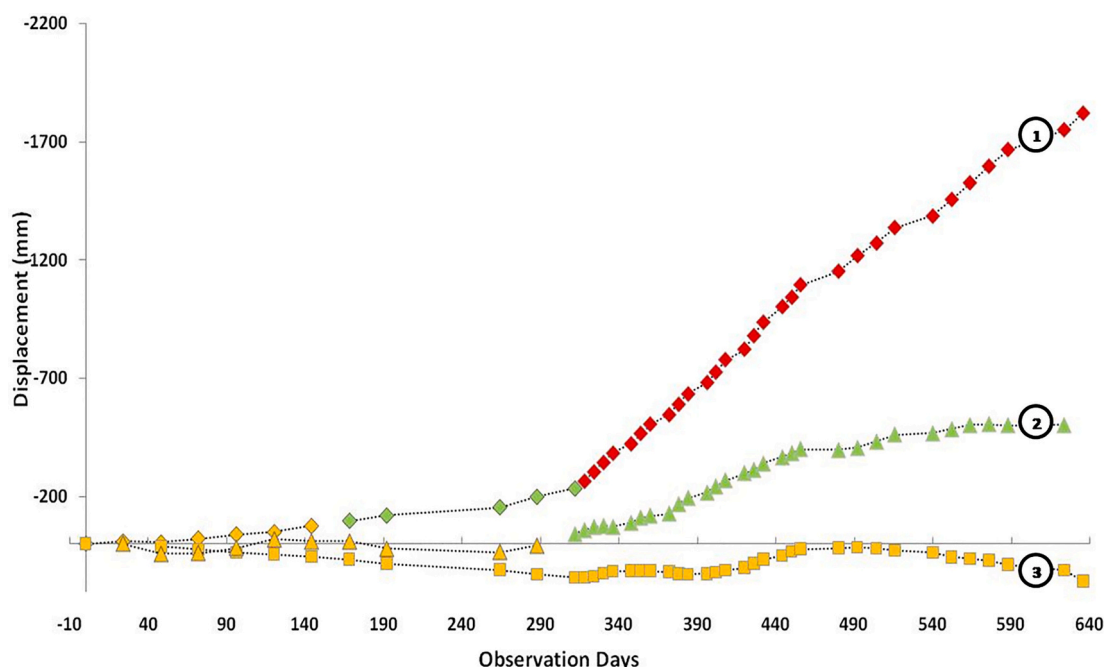


Fig. 4. The selection criterion of MPs representing characteristic displacements; 1: Accelerating MP; 2: Stable MP; 3: Un-deformed MP. The segments of the displacement curves are classified into: primary (yellow), secondary (green) and tertiary (red) creep stages. (For interpretation of the references to colour in this figure legend, the reader is referred to the web version of this article.)

and MIV, it is essential to identify the OOA of the slope material (herein MPs) prior to failure. This is identified by the break-in slope of the displacement time series graph immediately prior to failure. In the case of Kikruma, we present two representative MPs from the crown and flank of the landslide (MP 1 and MP 2). We identify the OOA to be on observation day number 444 (corresponding to 8 June 2018) i.e. 51 days prior to failure for the crown and day number 468 (corresponding to 2 July 2018) i.e. 27 days prior to failure for the flank. Using the INV, the trend line of the inverse velocity points from the MP 1 of the landslide intersects the time axis on observation day 492 (corresponding to 26 July 2018) with $R^2 = 0.57$. Similarly, the trend line of the inverse velocity points from MP 2 of the landslide intersects the time axis on observation day 493 (corresponding to 27 July 2018) with $R^2 = 0.87$.

On the other hand, for MP1, we implemented the MIV, with t_0 as 444 and t as 492 (see Eq. (1)) to estimate the time of failure, t_f to be on day

499 (corresponding to 2 August 2018), using the respective inverse velocity value ($1/v_0$ and $1/v$, Fig. 5). Accordingly, for MP 2 on the flank, we estimate t_0 as 468 with t as 492 to estimate the time of failure, t_f to be on day 495 (corresponding to 29 July 2018).

For the Kotropi landslide, the OOA is identified to be on observation day number 624 (corresponding to 31 July 2017) i.e. 13 days prior to actual failure in the PS and SBAS displacement time series. We demonstrate two MPs (MP 3 and MP4) in the crown region estimated from PS and SBAS, respectively and one MP (MP 5) at the flank of the landslide estimated from SBAS (Fig. 3b). Using the INV, for MP 3, the trend line of the inverse velocity points intersects the time axis on observation day 637 (corresponding to 13 August 2017). For MP 4 and MP 5 this corresponds to day 638 (corresponding to 14 August 2017). Using the MIV, considering the OOA to be 31 July 2017, we assume observation day 624 as t_0 , using the respective inverse velocity value ($1/$

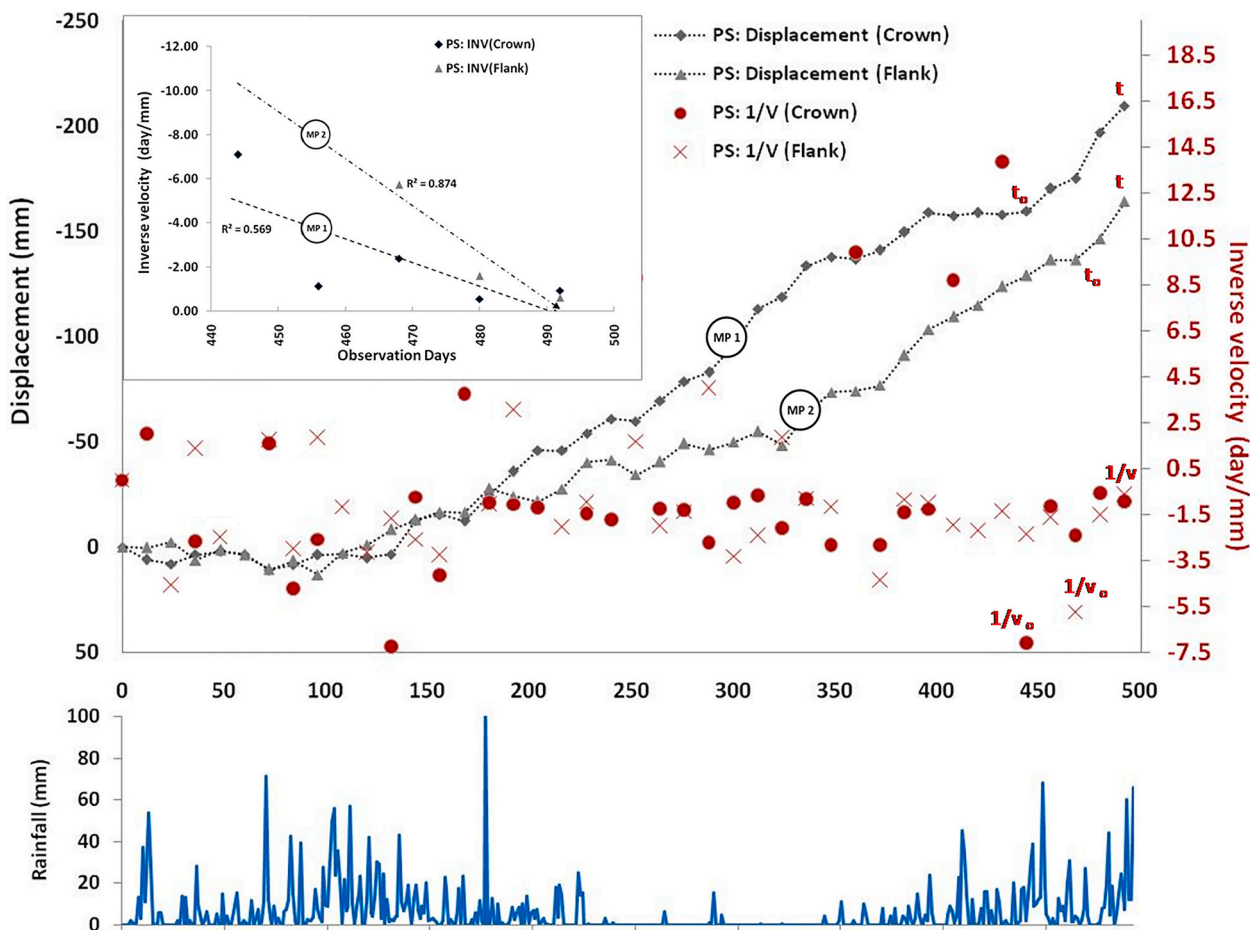


Fig. 5. Top panel: Representative displacement time series and inverse velocities for the Kikruma landslide showing the OOA (t_0) and last observation point (t). Inset: Failure day estimation using INV. Bottom panel: Rainfall variation in the region during the observation period.

v_0), using Eq. (1), we estimate the time of failure to be observation day 638 (which is 14 August 2017, Fig. 6 top panel) for all the three MPs. The displacement time series for both the landslides are correlated to the rainfall variation during the observation period (Figs. 5 and 6, bottom panel). It is worthwhile to mention here that, of all the MPs, only few exhibited the tertiary acceleration pattern correlated to rainfall.

4.3. Prediction of flow path

We ingested the information, derived from the cluster of accelerating MPs into the RAMMS simulation setup, as possible release areas (RA) from which the failure may have been initiated. The acceleration values were interpolated to create a “material acceleration image” of the landslide affected slope (Fig. 7a and b). The acceleration image is then classified into zones of high, medium and low acceleration based on image segmentation using Histogram-based thresholding with natural breaks (Fig. 7c and d). For Kikruma landslide, the threshold between low to medium acceleration is 0.024 dm/day^2 and that between medium to high is 0.39 dm/day^2 . Similarly for the Kotropi landslide, the threshold between low to medium acceleration is 0.30 dm/day^2 and that between medium to high is 0.69 dm/day^2 . The classified maps clearly show the zones of acceleration and their possible influence areas. For Kotropi, the initiation clearly starts from the upslope following a channel and gets deposited along the downslope, therefore, the RA has been considered from the upslope above MP5 which shows OOA leading to failure (Fig. 7e). Similarly, for Kikruma, high acceleration zones in the upslope areas above MP2, was considered as release area (Fig. 7f). Demarcation of release areas in both cases was guided by break-in slope as

morphological criteria, which is generally used to map landslide crown (Schlögel et al., 2015) (Fig. 7e and f).

The block depths for the individual RAs were estimated from the area-volume relationship as shown in Eq. (2). The finalised block depths of RAs for Kotropi and Kikruma landslides were estimated as 7m and 8 m, respectively.

The output flow path and the actual landslide boundary are intersected to estimate the Bf, Mf and detection percentage; this indicates the accuracy of the simulation (Fig. 8 and Table 1). In the case of Kikruma, the simulated release volume is $\sim 552,000 \text{ m}^3$ with a maximum flow velocity of 23.9 m/s and maximum flow height of 32.2 m. For Kotropi, the simulated release volume is $\sim 160,000 \text{ m}^3$ with a maximum flow velocity of 21.6 m/s and a maximum flow height of 27.3 m.

5. Discussion

We present a methodology for time and path prediction of landslides using PSI and SBAS (from Sentinel-1 data) and Voellmy flow model. The PSI and SBAS methods are utilised to generate displacement time series of the slope material representing individual MPs. Noise reduction and PS consistency are achieved using adequately long time series of data (Kovács et al., 2019). We have processed a time series Sentinel-1 data spanning ~ 1.5 years for Kikruma and 2 years for Kotropi with more than 40 scenes in each case. Further, the $|r|$ value of the representative MPs range from 5 to 18, which indicates that $|r| < 100$, thus demonstrating their reliability. It is to be noted that, the methodology adopted is not a combined PSI-SBAS method but the results from both of the independent techniques. The PSI method generated significant MPs distributed over

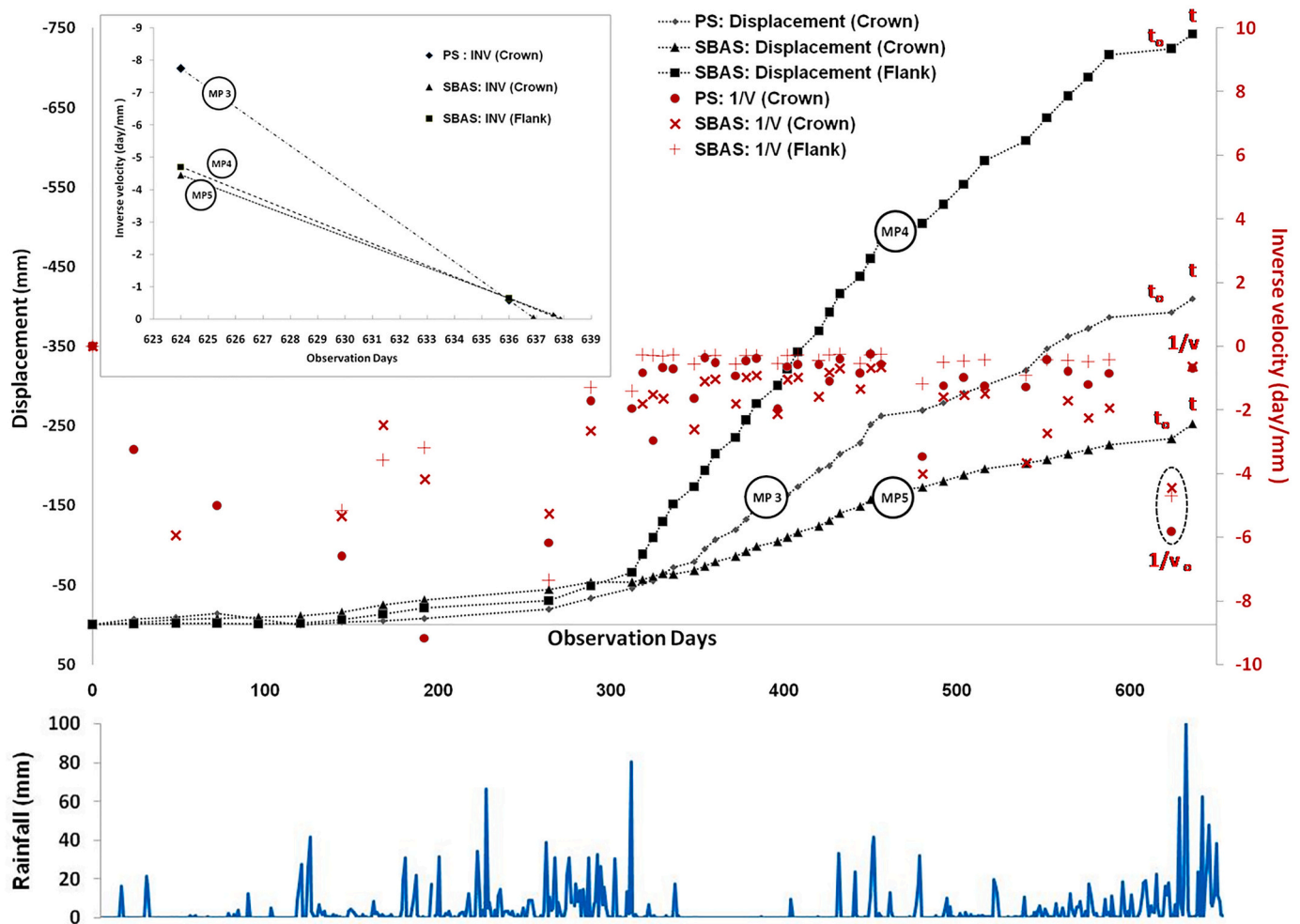


Fig. 6. Top panel: Displacement time series and inverse velocities for the Kotropi landslide showing the OOA (t_0) and last observation point (t). Inset: Failure day estimation using INV method. Bottom panel: Rainfall variation in the region during the observation period.

both the landslide areas. However, the SBAS method resulted in sparse clusters of MPs for Kotropi and no MP for Kikruma. The Kotropi landslide had pre-failure bare rock patches which acted as distributed targets in SBAS. However, the relatively high vegetation cover in the case of Kikruma prohibited coherent distributed targets even though point targets such as isolated open rocks were identified as PS (Chen et al., 2021).

The sign conventions of positive and negative displacements are a function of satellite and target distance wherein positive and negative values indicate decrease and increase in distance, respectively. In landslide kinematics, both are possible depending upon topography and failure type (refer Fig. 1 of Schlögel et al., 2015). In the present case, our representative MPs have negative values, indicating increase in satellite and target distance due to mainly a rotational type of failure near the crown in tertiary deformation stage. Comparison of the velocities between ascending and descending InSAR measurements of the same sensors is a common practice checking the consistency of estimates (Aslan et al., 2019). We have carried out the same for the Kotropi landslide and it is seen that the velocity distribution is comparable, as generally found in steep slopes with active deformation (Supplementary material 2). However, similar analysis could not be carried out for Kikruma landslide due to unavailability of data in descending pass.

The trend of the time series is analysed to identify the locations along the trend line where the material is accelerating and thus will lead to eventual failure during an effective trigger. Further, the pattern of the displacement time series also throws light on the kinematics of the

individual landslides (Petley et al., 2002 and Petley et al., 2005, Dick et al., 2015). The pre-failure trends as seen from the cumulative displacement plots for both Kikruma and Kotropi landslides, exhibit a transitional and rotational type of movement (Dick et al., 2015). This implies periodic intervals of stability followed by an accelerated movement induced by a triggering factor, herein rainfall. Petley et al. (2005) classified such movements to be “Type 1” primarily associated with areas around crown with the movement pattern consisting of slow creep with intermittent acceleration induced by rainfall.

The displacement time series for the Kikruma landslide shows the initiation of slope instability from August 2017 which is almost a year prior to the actual failure. The OOA was observed on 8 June 2018 for the representative MP on the crown and 2 July 2018 on the flank. From these, using INV and MIV we have predicted the day of failure to be 26 July 2018 and 2 August 2018 for the crown, and 27 July 2018 and 29 July 2018 for the flank, respectively (Table 2). Herein the actual day of failure is 29 July 2018. Similarly, using PSI and SBAS methods, for the Kotropi landslide, the initiation of instability was recorded during August 2016 with the OOA observed on 31 July 2017 for all MPs located in the crown and flank. Using PSI (MP 3), the INV and the MIV predicted the day of failure as 13 and 14 August 2017, respectively on the crown, whereas using SBAS, both INV and MIV predicted the day of failure to be 14 August 2017 for MP 4 and MP 5 on the crown and flank, respectively (Table 2). The actual day of failure is 13 August 2017.

We attempted to corroborate the displacement pattern and OOA day to the physical triggering factor, herein rainfall. This will further

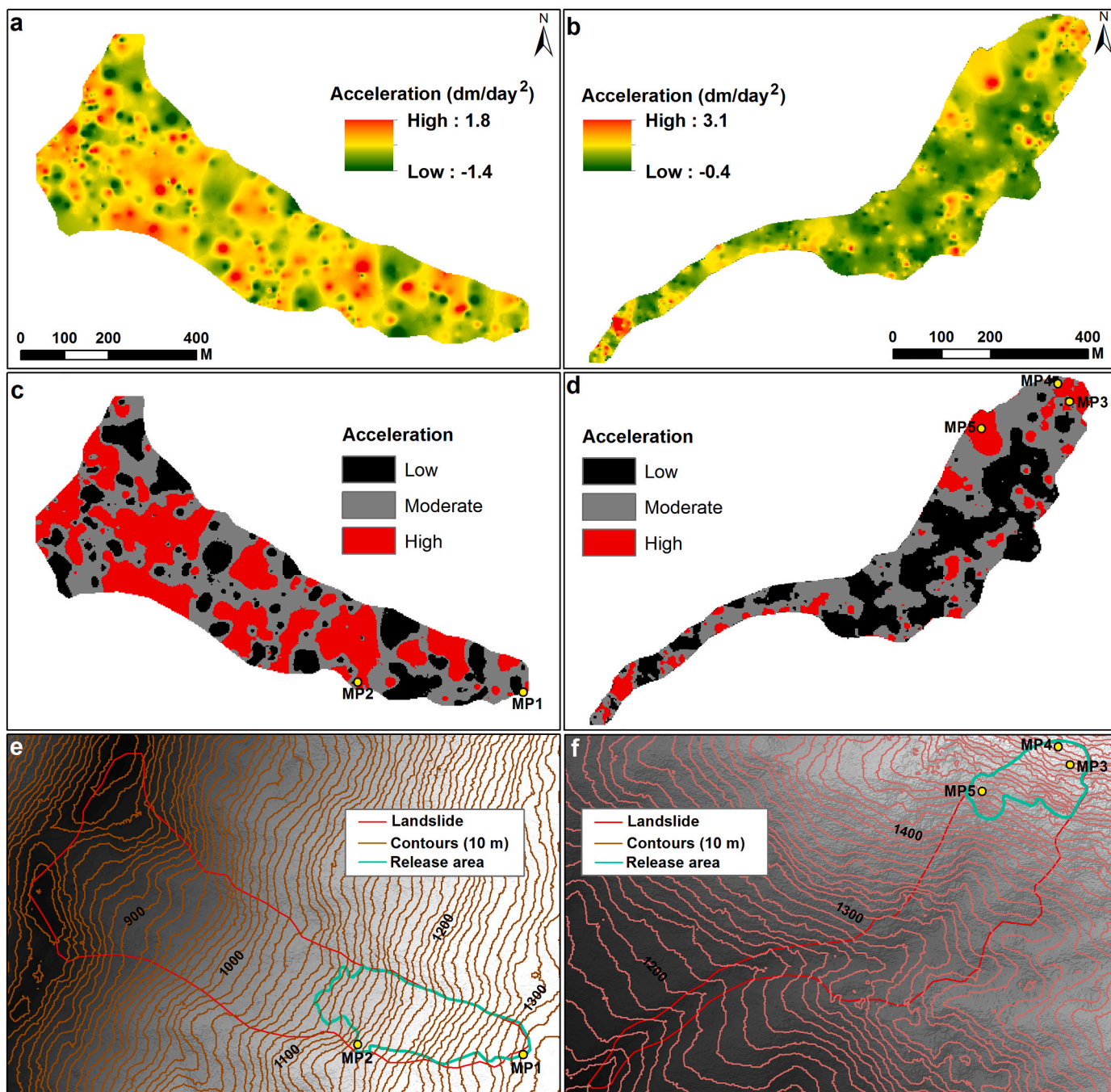


Fig. 7. Material acceleration map for a. Kikruma and b. Kotropi landslides; Classified acceleration maps for c. Kikruma and d. Kotropi landslides and Release area maps for e. Kikruma and f. Kotropi landslides.

substantiate the selection of OOA and robustness of the prediction vis-a-vis the displacement time series. The slope destabilization for the Kikruma landslide was initiated on 14 September 2017 (observation day 177). There was a heavy rainfall of approximately 100 mm in and around that region on that day which may have triggered the beginning of destabilization. The OOA at the crown of the Kikruma landslide was identified on 8 June 2018 (observation day 444). Observation from the CPC precipitation data shows that although 8 June 2018 recorded scanty rainfall, the preceding days of 6 and 7 June 2018 recorded antecedent rainfall of ~66 mm thereby triggering the acceleration which was recorded on 8 June 2018. However, another spell of high rainfall was recorded around 2 July 2018 which may have resulted in OOA on the flanks. This observation demonstrates an unsteady acceleration pattern

controlled by rainfall leading to the landslide failure. For the Kotropi landslide, the slope de-stabilization was initiated around 10 September 2016 (observation day 300). The recorded rainfall for that period is ~100 mm which may have led to the beginning of destabilization (Fig. 6). The OOA was identified on 31 July 2017 (observation day 624). The precipitation information reveals that the region experienced a considerable amount of rainfall i.e. ~ 62 mm on 31 July 2017 which is almost four times the average rainfall of the preceding 10 days (~ 15 mm). This rainfall event may have triggered the final acceleration leading to failure.

We demonstrated the usability of INV and MIV in failure prediction of landslides. We observed that in both cases the INV predicts the failure on the day or few days prior to actual failure. This prediction thus acts as

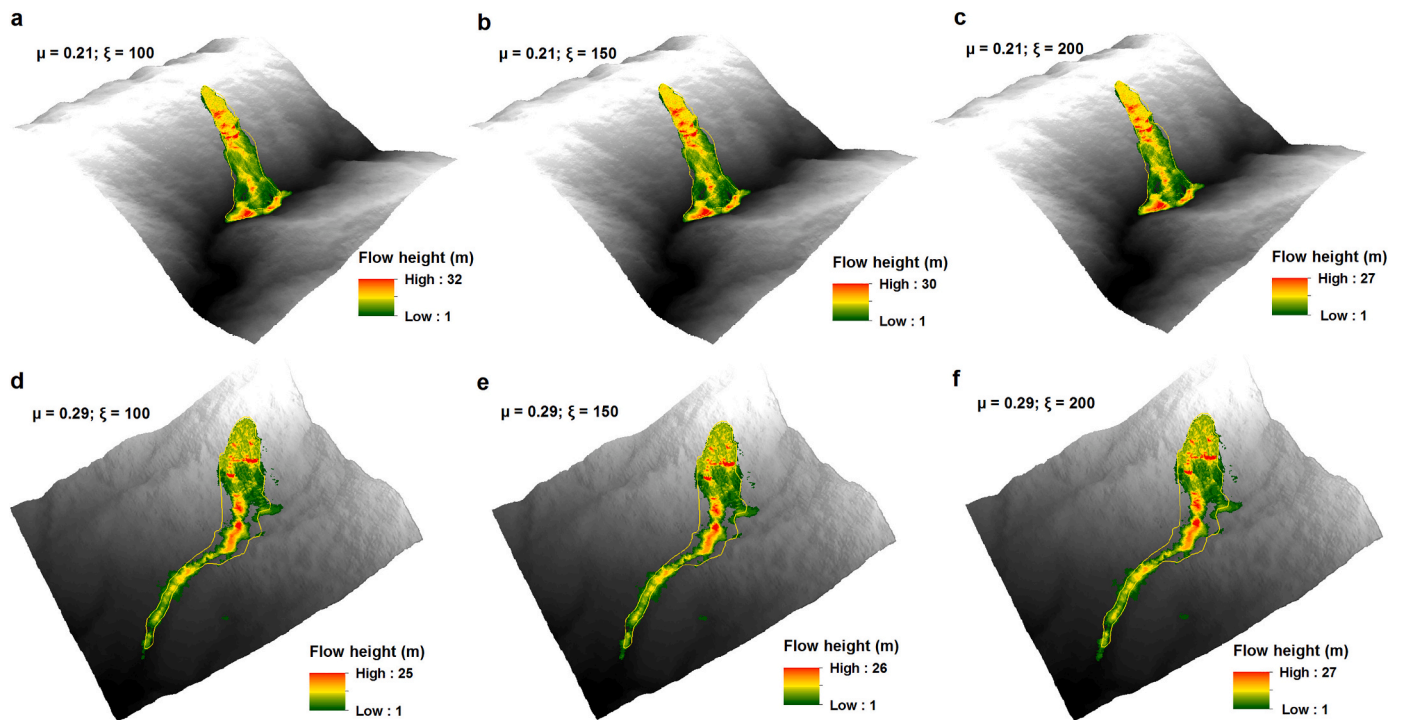


Fig. 8. a-c: Simulated flow height for Kikruma landslide. d-e: Simulated flow height for Kotropi landslide.

Table 1

Iterations incorporated in RAMMS with different values of ξ for both the debris flows and respective accuracy estimates.

		Dry-Coulomb (μ)	Viscous-Turbulent (ξ)	Branching Factor (Bf)	Miss factor (Mf)	Detection Percentage
Kikruma	Iteration 1	0.21	100	0.19	0.06	94.1
	Iteration 2		150	0.19	0.07	93.6
	Iteration 3		200	0.20	0.07	93.2
Kotropi	Iteration 1	0.29	100	0.23	0.26	79.1
	Iteration 2		150	0.22	0.26	79.2
	Iteration 3		200	0.21	0.26	79.4

Table 2

Prediction of failure day from INV and MIV.

Landslide	Measurement Point	Actual Day of failure	PREDICTED DAYS OF FAILURE	
			INV	MIV
Kikruma	MP1	29 July 2018	26 July 2018	2 August 2018
	MP2		27 July 2018	29 July 2018
	MP3		13 August 2017	14 August 2017
Kotropi	MP4	13 August 2017	14 August 2017	14 August 2017
	MP5		14 August 2017	14 August 2017

a safe prediction. The MIV has predicted the failure after the day of actual failure therefore categorizing it as an unsafe prediction. Precise prediction of the day of failure, using the standalone methods are debatable as it does not take into account natural uncertainties and thus are unrealistic. We, therefore, recommend the usage of both INV and MIV to ascertain a time window of failure (in days) in which the actual slope failure may occur.

In addition to the prediction of failure, we have also modelled the probable geometry and flow path of the landslides. We have segmented the acceleration image generated from PS and SBAS MPs to identify the release area from where the slope material may collapse. This is a new method proposed to estimate release area from displacement time series derived from InSAR. Using these release areas for both the landslides, we have simulated the flow in RAMMS using values of internal and external friction. The simulated model showed a good match with the actual

failure (Table 1). We have broadly benchmarked the outcomes presented by RAMMS with two other probabilistic/empirical and Voellmy model based debris flow simulation algorithms i.e. Debris flow predictor (Guthrie and Befus, 2021) and R.avaflow (Mergili et al., 2017), respectively. The results demonstrated that RAMMS show a good match with the actual flow geometry (Supplementary material 3). The mismatches within the RAMMS simulation outcomes, wherever seen is due to the inaccurate representation of the topography by the DEM used owing to the constraints of spatial resolution. Minor and local variations in topography are not represented accurately by coarse resolution DEM but have a control in the overall flow morphology. We verified this by performing sensitivity analysis using CartoDEM of 2.5 m, 5 m, 10 m and 20 m spatial resolution (Supplementary Material 4). Further, the selection of modelling parameters i.e. μ and ξ , and consideration of the quantity of precipitation, shows a significant control on the prediction of

outcomes. As mentioned earlier, the failure zone of the Kotropi landslide is composed of fine-grained mudstones, as compared to the sandstones and quartzites of Kikruma in the eastern Himalayas. Coupled with heavy rainfall, the slope material in Kotropi behaved in a much more fluidized form in contrast to Kikruma. The accuracy of the prediction results are estimated in terms of flow branching factor and high detection percentage. For Kotropi landslide, the lowest Bf (0.21) and highest detection percentage (79%) is observed when μ is 0.29 and ξ is 200 (Table 1). In contrast, for Kikruma, the lowest Bf (0.19) and highest detection percentage (94%) is observed with the combination of μ being 0.21 and ξ being 100 (Table 1). This shows the granular nature of the debris flow with less moisture content since the rainfall impact was lower in this region. We, therefore recommend careful consideration of slope material and amount of precipitation prior to failure in the flow modelling exercise.

It is worthwhile to mention here that the simulation setup is currently carried out with apriori knowledge of the landslide. However, in a forecast scenario, the identification of RAs from accelerating MPs using PSI and SBAS may enable simulation of the failure, with iterative and multiple boundary conditions (depths, coefficients etc.). This presents a probabilistic idea about the extent of the failure, its possible geometry and the damage it may cause to any associated establishments.

6. Conclusion

In this work, we present a methodology for prediction of the time and path of landslide using analysis of Kikruma and Kotropi landslides as the test cases. The slopes on which the failures occurred were analysed using the PSI and SBAS approaches with 42 Sentinel-1 SAR images. The resultant displacement-time series highlighted the presence of active movements on the head scarp region of both the landslides prior to failure. The instability has commenced almost a year prior to failure in both landslide instances. This is evident from the displacement time series derived from the MPs. We used the INV and MIV derived from the displacement estimates to forecast the window of failure. The deformation-time series and predicted day of failure are in good agreement from the different locations in PSI as well as SBAS methods. Precise identification of the time of OOA supported by evidence from triggering factors (i.e. rainfall) is essential for accurate landslide early warning. The cluster and distribution of accelerating MPs provide information about the possible locations of release areas. This information can be ingested into the RAMMS environment to model the landslide flow using appropriate frictional coefficients to estimate the path of the landslide and the extent of failure and damage. Due to the regularity in the acquisition of SAR imagery from Sentinel-1 satellites, it is now possible to continuously monitor ground deformation in a region. We were able to utilise Sentinel-1 data with a 12-day interval for our study area. However, the data are available in 6-day repetivity for other regions which will further improve identification of OOA. This integrated with mathematical methods such as inverse and modified inverse velocity methods and numerical simulation such as RAMMS can forecast the occurrence and geometry of a landslide in time and space.

Declaration of Competing Interest

The authors declare that they have no known competing financial interests or personal relationships that could have appeared to influence the work reported in this paper.

Acknowledgements

This work is the outcome of the Technology Development Project (TDP) of NRSC. We thank Deputy Director (RSA) and Director, NRSC for their support and guidance. We thank Stantec for providing us the demo license of Debris flow predictor. We also thank Dr. Martin Mergilli for providing us the R.avaflo code. We thank three anonymous reviewers

and Dr. Joseph Awange (Associate Editor) for their suggestions which helped us to improve the paper.

Appendix A. Supplementary data

Supplementary data to this article can be found online at <https://doi.org/10.1016/j.rse.2022.112899>.

References

- Amelung, F., Oppenheimer, C., Segall, P., Zebker, H., 2000. Ground deformation near Gada 'Ale volcano, Afar, observed by radar interferometry. *Geophys. Res. Lett.* 27 (19), 3093–3096.
- Aslan, G., Cakir, Z., Lasserre, C., Renard, F., 2019. Investigating subsidence in the Bursa plain, Turkey, using ascending and descending Sentinel-1 satellite data. *Remote Sens.* 11 (1), 85. <https://doi.org/10.3390/rs11010085>.
- Ayotte, D., Hungr, O., 2000. Calibration of a Runout Prediction Model for Debris Flow and Naeser, Rotterdam, pp. 505–514.
- Bekaert, D.P.S., Handwerker, A.L., Agram, P., Kirschbaum, D.B., 2020. InSAR-based detection method for mapping and monitoring slow-moving landslides in remote regions with steep and mountainous terrain: an application to Nepal. *Remote Sens. Environ.* 249, 111983 <https://doi.org/10.1016/j.rse.2020.111983>.
- Berardino, P., Fornaro, G., Lanari, R., Sansosti, E., 2002. A new algorithm for surface deformation monitoring based on small baseline differential SAR interferograms. *IEEE Trans. Geosci. Remote Sens.* 40, 2375–2383. <https://doi.org/10.1109/tgrs.2002.803792>.
- Berger, C., 2010. Debris Flow Entrainment and Sediment Transfer Processes at the Illgraben Catchment, Switzerland. Ph.D. thesis. University of Bern, Inst. of Geological Sciences, Bern, Switzerland.
- Berger, C., McArdell, B.W., Schlunegger, F., 2011. Direct measurement of channel erosion by debris flows, Illgraben, Switzerland. *J. Geophys. Res. Earth Surf.* 116, F01002. <https://doi.org/10.1029/2010JF001722>.
- Boni, R., Bordoni, M., Colombo, A., Lanteri, L., Meisina, C., 2018. Landslide state of activity maps by combining multi-temporal A-DInSAR (λ). *Remote Sens. Environ.* 217, 172–190. <https://doi.org/10.1016/j.rse.2018.08.013>.
- Bovis, M.J., Jakob, M., 1999. The role of debris supply conditions in predicting debris flow activity. *Earth Surf. Process. Landf.* 24, 1039–1054. [https://doi.org/10.1002/\(sici\)1096-9837\(199910\)24\(10\)1039::AID-ESP1039>3.0.CO;2-1](https://doi.org/10.1002/(sici)1096-9837(199910)24(10)1039::AID-ESP1039>3.0.CO;2-1).
- Bui, L.K., Featherstone, W.E., Filmer, M.S., 2020. Disruptive influences of residual noise, network configuration and data gaps on InSAR-derived land motion rates using the SBAS technique. *Remote Sens. Environ.* 247, 111941 <https://doi.org/10.1016/j.rse.2020.111941>.
- Bui, L.K., Le, P.V.V., Dao, P.D., Long, N.Q., Pham, H.V., Tran, H.H., Xie, L., 2021. Recent land deformation detected by sentinel-1A InSAR data (2016–2020) over Hanoi, Vietnam, and the relationship with groundwater level change [article]. *GISci. Remote Sens.* 58 (2), 161–179. <https://doi.org/10.1080/15481603.2020.1868198>.
- Bürgmann, R., Rosen, P.A., Fielding, E.J., 2000. Synthetic aperture radar interferometry to measure Earth's surface topography and its deformation. *Annu. Rev. Earth Planet. Sci.* 28 (1), 169–209.
- Carla, T., Farina, P., Intrieri, E., Ketizmen, H., Casagli, N., 2018. Integration of ground-based radar and satellite InSAR data for the analysis of an unexpected slope failure in an open-pit mine. *Eng. Geol.* 235, 39–52. <https://doi.org/10.1016/j.enggeo.2018.01.021>.
- Carnece, C., Massonnet, D., King, C., 1996. Two examples of the use of SAR interferometry on displacement fields of small spatial extent. *Geophys. Res. Lett.* 23, 3579–3582. <https://doi.org/10.1029/96gl03042>.
- Casu, F., Manzo, M., Lanari, R., 2006. A quantitative assessment of the SBAS algorithm performance for surface deformation retrieval from DInSAR data. *Remote Sens. Environ.* 102 (3–4), 195–210. <https://doi.org/10.1016/j.rse.2006.01.023>.
- Chen, X., Tessari, G., Fabris, M., Achilli, V., Floris, M., 2021. Comparison between PS and SBAS InSAR techniques in monitoring shallow landslides. In: *Workshop on World Landslide Forum*, November (pp. 155–161). Springer, Cham. https://doi.org/10.1007/978-3-030-60311-3_17.
- Cigna, F., Bianchini, S., Casagli, N., 2013. How to assess landslide activity and intensity with persistent scatterer interferometry (psi): the psi-based matrix approach. *Landslides* 10, 267–283. <https://doi.org/10.1007/s10346-012-0335-7>.
- Crippa, C., Valbuzzi, E., Frattini, P., Crosta, G.B., Spreafico, M.C., Agliardi, F., 2021. Semi-automated regional classification of the style of activity of slow rock-slope deformations using PS InSAR and SqueeSAR velocity data. *Landslides* 1–19. <https://doi.org/10.5194/egusphere-egu21-8392>.
- Crosta, G.B., Agliardi, F., 2003. Failure forecast for large rock slides by surface displacement measurements. *Can. Geotech. J.* 40, 176–191. <https://doi.org/10.1139/t02-085>.
- Del Soldato, M., Riquelme, A., Bianchini, S., Tomàs, R., Di Martire, D., De Vita, P., Moretti, S., Calcaterra, D., 2018. Multisource data integration to investigate one century of evolution for the Agnone landslide (Molise, southern Italy). *Landslides* 15, 2113–2128. <https://doi.org/10.1007/s10346-018-1015-z>.
- Dick, G.J., Eberhardt, E., Cabrejo-Liévano, A.G., Stead, D., Rose, N.D., 2015. Development of an early-warning time-of-failure analysis methodology for open-pit mine slopes utilizing ground-based slope stability radar monitoring data. *Can. Geotech. J.* 52 (4), 515–529. <https://doi.org/10.1139/cgj-2014-0028>.
- Dong, J., Zhang, L., Tang, M., Liao, M., Xu, Q., Gong, J., Ao, M., 2018. Mapping landslide surface displacements with time series SAR interferometry by combining persistent

- and distributed scatterers: a case study of Jiayu landslide in Danba, China. *Remote Sens. Environ.* 205, 180–198. <https://doi.org/10.1016/j.rse.2017.11.022>.
- Dun, J., Feng, W., Yi, X., Zhang, G., Wu, M., 2021. Detection and mapping of active landslides before in the Baihetan reservoir area (China) based on the time-series InSAR method. *Remote Sens.* 13, 3213. <https://doi.org/10.3390/rs13163213>.
- Ferretti, A., Prati, C., Rocca, F., 2001. Permanent scatterers in SAR interferometry. *IEEE Trans. Geosci. Remote Sens.* 39, 8–20. <https://doi.org/10.1109/36.868878>.
- Ferretti, A., Savio, G., Barzaghi, R., Borghi, A., Musazzi, S., Novali, F., Rocca, F., 2007. Submillimeter accuracy of InSAR time series: experimental validation. *IEEE Trans. Geosci. Remote Sens.* 45 (5), 1142–1153. <https://doi.org/10.1109/tgrs.2007.894440>.
- Froude, M.J., Petley, D.N., 2018. Global fatal landslide occurrence from 2004 to 2016. *Nat. Hazards Earth Syst. Sci.* 18, 2161–2181. <https://doi.org/10.5194/nhess-18-2161-2018>.
- Fukuzono, T., 1985a. A method to predict the time of slope failure caused by rainfall using the inverse number of velocities of surface displacement. *Landslides*. 22 (2) <https://doi.org/10.3313/jls1964.22.2.8>, 8–13.1.
- Fukuzono, T., 1985b. A new method for predicting the failure time of a slope. In: *Proceedings of the 4th International Conference and Field Workshop on Landslides Tokyo*. Tokyo University Press, pp. 145–150.
- García-Davalillo, J.C., Herrera, G., Notti, D., Strozzi, T., Álvarez-Fernández, I., 2014. DInSAR analysis of ALOS PALSAR images for the assessment of very slow landslides: the Tena valley case study. *Landslides* 11, 225–246. <https://doi.org/10.1007/s10346-012-0379-8>.
- Goldstein, R.M., Werner, C.L., 1998. Radar interferogram filtering for geophysical applications. *Geophys. Res. Lett.* 25 (21), 4035–4038. <https://doi.org/10.1029/1998gl900033>.
- GSI, 2018. Preliminary Post Disaster Study of the Landslide at Kikruma (on Left Bank Slope of Sidzu River), Phek District, Nagaland. Geological Survey of India, Northeastern Region.
- Guthrie, R., Befus, A., 2021. DebrisFlow predictor: an agent-based runoff program for shallow landslides. *Nat. Hazards Earth Syst. Sci.* 21 (3), 1029–1049. <https://doi.org/10.5194/nhess-21-1029-2021>.
- Herrera, G., Notti, D., García-Davalillo, J.C., Mora, O., Cooksley, G., Sánchez, M., Arnaud, A., Crossetto, M., 2011. Analysis with C-and X-band satellite SAR data of the Portalet landslide area. *Landslides* 8, 195–206. <https://doi.org/10.1007/s10346-010-0239-3>.
- Hu, X., Burgmann, R., Fielding, E.J., Lee, H., 2020a. Internal kinematics of the Slumgullion landslide (USA) from high-resolution UAVSAR InSAR data. *Remote Sens. Environ.* 251, 112057 <https://doi.org/10.1016/j.rse.2020.112057>.
- Hu, X., Bürgmann, R., Schulz, W.H., Fielding, E.J., 2020b. Four-dimensional surface motions of the Slumgullion landslide and quantification of hydrometeorological forcing. *Nat. Commun.* 11 (1), 1–9. <https://doi.org/10.1038/s41467-020-16617-7>.
- Intrieri, E., Raspini, F., Fumagalli, A., Lu, P., Del Conte, S., Farina, P., Allievi, J., Ferretti, A., Casagli, N., 2017. The Maoxian landslide as seen from space: detecting precursors of failure with Sentinel-1 data. *Landslides* 15, 123–133. <https://doi.org/10.1007/s10346-017-0915-7>.
- Kampes, B.M., Hanssen, R.F., 2004. Ambiguity resolution for permanent scatterer interferometry. *IEEE Trans. Geosci. Remote Sens.* 42, 2446–2453. <https://doi.org/10.1109/tgrs.2004.835222>.
- Khaki, M., Filmer, M.S., Featherstone, W.E., Kuhn, M., Bui, L.K., Parker, A.L., 2020. A sequential Monte Carlo framework for noise filtering in InSAR time series. *IEEE Trans. Geosci. Remote Sens.* 58 (3), 1904–1912. <https://doi.org/10.1109/TGRS.2019.2950353>.
- Kovács, I.P., Bugya, T., Czigány, S., Defilippi, M., Lóczy, D., Riccardi, P., Ronczyk, L., Pasquali, P., 2019. How to avoid false interpretations of sentinel-1A TOPSAR interferometric data in landslide mapping? A case study: recent landslides in Transdanubia, Hungary. *Nat. Hazards* 96 (2), 693–712. <https://doi.org/10.1007/s11069-018-3564-9>.
- Kumar, V., Gupta, V., Jamir, I., Chattoraj, S.L., 2018. Evaluation of potential landslide damming: case study of Urni landslide, Kinnaur, Satluj valley, India. *Geosci. Front.* 10 (2), 753–767. <https://doi.org/10.1016/j.gsf.2018.05.004>.
- Larsen, L.J., Montgomery, D.R., Korup, O., 2010. Landslide erosion controlled by hillslope material. *Nat. Geosci.* 3, 247–251. <https://doi.org/10.1038/ngeo776>.
- Lauknes, T.R., Zebker, H.A., Larsen, Y., 2011. InSAR deformation time series using an L1-norm small-baseline approach. *IEEE Trans. Geosci. Remote Sens.* 49 (1), 536–546. <https://doi.org/10.1109/tgrs.2010.2051951>.
- Lee, D.S., Shan, J., Bethel, J.S., 2003. Class-guided building extraction from Ikonos imagery. *Photogramm. Eng. Remote Sens.* 69 (2), 143–150. <https://doi.org/10.14358/pers.69.2.143>.
- Lu, P., Casagli, N., Catani, F., Tofani, V., 2012. Persistent scatterers interferometry hotspot and cluster analysis (PSI-HCA) for detection of extremely slow-moving landslides. *Int. J. Remote Sens.* 33, 466–489. <https://doi.org/10.1080/01431161.2010.536185>.
- Luna, B.Q., Blahut, J., Kappes, M., Akbas, S.O., Malet, J.P., Remaître, A., Jaboyedoff, M., 2013. Methods for debris flow Hazard and risk assessment. *Adv. Nat. Technol. Hazards Res.* 133–177. https://doi.org/10.1007/978-94-007-6769-0_5.
- Martha, T.R., Kerle, N., Jetten, V., van Westen, C.J., Vinod Kumar, K., 2010a. Landslide volumetric analysis using cartosat-1-derived data. *IEEE Geosci. Remote Sens. Lett.* 7, 582–586. <https://doi.org/10.1109/LGRS.2010.2041895>.
- Martha, T.R., Kerle, N., van Westen, C.J., Jetten, V., Vinod Kumar, K., 2010b. Effect of sun elevation angle on dsms derived from cartosat-1 data. *Photogramm. Eng. Remote Sens.* 76, 429–438. <https://doi.org/10.14358/PERS.76.4.429>.
- Martha, T.R., Roy, P., Jain, N., Khanna, K., Mrinalni, K., Vinod Kumar, K., Rao, P.V.N., 2021. Geospatial landslide inventory of India - an insight into occurrence and exposure on a national scale. *Landslides* 18, 2125–2141. <https://doi.org/10.1007/s10346-021-01645-1>.
- Martha, T.R., Kerle, N., Van Westen, C.J., Jetten, V., Kumar, K.V., 2012. Object-oriented analysis of multi-temporal panchromatic images for creation of historical landslide inventories. *ISPRS journal of photogrammetry and remote sensing* 67, 105–119.
- Massonnet, D., Feigl, K.L., 1998. Radar interferometry and its application to changes in the earth's surface. *Rev. Geophys.* 36 (4), 441–500. <https://doi.org/10.1029/97rg03139>.
- Mergili, M., Fischer, J.T., Krenn, J., Pudasaini, S.P., 2017. r. Avaflow v1, an advanced open-source computational framework for the propagation and interaction of two-phase mass flows. *Geosci. Model Dev.* 10 (2), 553–569. <https://doi.org/10.5194/gmd-10-553-2017>.
- Mondini, A.C., Guzzetti, F., Channg, K.T., Monserrat, O., Martha, T.R., Manconi, A., 2021. Landslide failure detection and mapping using synthetic aperture radar: past, present and future. *Earth Sci. Rev.* 216, 103574 <https://doi.org/10.1016/j.earscirev.2021.103574>.
- Motagh, M., Walter, T.R., Sharifi, M.A., Fielding, E., Schenk, A., Anderssohn, J., Zschau, J., 2008. Land subsidence in Iran caused by widespread water reservoir overexploitation. *Geophys. Res. Lett.* 35 (16) <https://doi.org/10.1029/2008GL038814>.
- Mufundirwa, A., Fujii, Y., Kodama, J., 2010. A new practical method for prediction of geomorphological failure-time. *Int. J. Rock Mech. Min. Sci.* 47, 1079–1090. <https://doi.org/10.1016/j.ijrmms.2010.07.001>.
- Petley, D.N., 2013. Global losses from landslides associated with dams and reservoirs. In: *Genevois, R., Prestininzi, A. (Eds.), International Conference on Vajont – 1963-2013, Thoughts and Analyses after 50 since the Catastrophic Landslide*. Italian Journal of Engineering and Environment – Book Series N, vol. 6, pp. 63–72.
- Petley, D.N., Bulmer, M.H., Murphy, W., 2002. Patterns of movement in rotational and translational landslides. *Geology* 30 (8), 719–722. [https://doi.org/10.1130/0091-7613\(2002\)030%3C0719:pomira%3E2.0.co;2](https://doi.org/10.1130/0091-7613(2002)030%3C0719:pomira%3E2.0.co;2).
- Petley, D.N., Mantovani, F., Bulmer, M.H., Zannoni, A., 2005. The use of surface monitoring data for interpretation of landslide movement patterns. *Geomorphology* 66 (1–4), 133–147. <https://doi.org/10.1016/j.geomorph.2004.09.011>.
- Pradhan, S.P., Panda, S.D., Roul, A.R., Thakur, M., 2019. Insights into the recent Kotropi landslide of august 2017, India: a geological investigation and slope stability analysis. *Landslides* 16 (8), 1529–1537. <https://doi.org/10.1007/s10346-019-01186-8>.
- Prati, C., Ferretti, A., Perissin, D., 2010. Recent advances on surface ground deformation measurement by means of repeated space-borne SAR observations. *J. Geodyn.* 49 (3–4), 161. <https://doi.org/10.1016/j.jog.2009.10.011>.
- Raspini, F., Bianchini, S., Ciampalini, A., Del Soldato, M., Solari, L., Novali, F., Del Conte, S., Rucci, A., Ferretti, A., Casagli, N., 2018. Continuous, semi-automatic monitoring of ground deformation using sentinel-1 satellites. *Sci. Rep.* 8, 7253. <https://doi.org/10.1038/s41598-018-25369-w>.
- Rickenmann, D., 1999. Empirical relationships for debris flows. *Nat. Hazards* 19, 47–77.
- Righini, G., Pancioli, V., Casagli, N., 2012. Updating landslide inventory maps using persistent scatterer interferometry (PSI). *Int. J. Remote Sens.* 33, 2068–2096. <https://doi.org/10.1080/01431161.2011.605087>.
- Rose, N.D., Hung, O., 2007. Forecasting potential rock slope failure in open pit mines using the inverse-velocity method. *Int. J. Rock Mech. Min. Sci.* 44, 308–320. <https://doi.org/10.1016/j.ijrmms.2006.07.014>.
- Rosi, A., Tofani, V., Tanteri, L., Stefanelli, C.T., Agostini, A., Catani, F., Casagli, N., 2018. The new landslide inventory of Tuscany (Italy) updated with PS-InSAR: geomorphological features and landslide distribution. *Landslides* 15, 5–19. <https://doi.org/10.1007/s10346-017-0861-4>.
- Rott, H., Scheuchl, B., Siegel, A., Grasmann, B., 1999. Monitoring very slow slope movements by means of SAR interferometry: a case study from a mass waste above a reservoir in the Ötztal Alps, Austria. *Geophys. Res. Lett.* 26, 1629–1632. <https://doi.org/10.1029/1999gl900262>.
- Roy, P., Martha, T.R., Jain, N., Vinod Kumar, K., 2018. Reactivation of minor scars to major landslides - a satellite based analysis of Kotropi landslide (13 august 2017) in Himachal Pradesh, India. *Curr. Sci.* 115 (3), 395–398. <https://doi.org/10.18520/cs/v115/i3/395-398>.
- Saito, M., 1996. Forecasting time of slope failure by tertiary creep. In: *Proceedings of the 7th International Conference on Soil Mechanics and Foundation Engineering* (pp. 2: 677–683).
- Salm, B., 1993. Flow, flow transition and runoff distances of flowing avalanches. *Ann. Glaciol.* 18, 221–226. <https://doi.org/10.1017/s0260305500011551>.
- Salm, B., Burkard, A., Gubler, H., 1990. Berechnung von Fliesslawinen: eineAnleitungfürPraktikermitBeispielen. *Mitteilung 47, Eidg. InstitutfürSchnee- und Lawinenforschung SLF*.
- SARMAP, 2012. SARscape: Technical Description. SARMAP, Purasca, Switzerland.
- Schlögel, R., Doube, C., Malet, J.P., Masson, F., 2015. Landslide deformation monitoring with ALOS/PALSAR imagery: a D-InSAR geomorphological interpretation method. *Geomorphology* 15 (231), 314–330. <https://doi.org/10.1016/j.geomorph.2014.11.031>.
- Schraml, K., Thomschitz, B., Graf, Mc Ardell B., Ckainra, R., 2015. Modeling debris-flow runoff patterns on two alpine fans with different dynamic simulation models. *Nat. Hazards Earth Syst. Sci.* 15 <https://doi.org/10.5194/15-1483-2015>, 10.5194/nhess-15-1483-2015.
- Sharma, A., Kartikyan, D., 2014. Potential of CartoDEM in disaster management. *J. Geom.* 8, 96–100.
- Shufelt, J.A., 1999. Performance evaluation and analysis of monocular building extraction from aerial imagery. *IEEE Trans. Pattern Anal. Mach. Intell.* 21 (4), 311–326. <https://doi.org/10.1109/34.761262>.

- Singh Roy, V., Mattar, K.E., Gray, A., 1998. Landslide characterisation in Canada using interferometric SAR and combined SAR and TM images. *Adv. Space Res.* 21 (3), 465–476. <https://doi.org/10.4095/219148>.
- Strozzi, T., Farina, P., Corsini, A., Ambrosi, C., Thüring, M., Zilger, J., Wiesmann, A., Wegmüller, U., Werner, C., 2005. Survey and monitoring of landslide displacements by means of InSAR satellite SAR interferometry. *Landslides* 2, 193–201. <https://doi.org/10.1007/s10346-005-0003-2>.
- Tang, C., Zhu, J., Chang, M., Ding, J., Qi, X., 2012. An empirical-statistical model for predicting debris-flow runout zones in the Wenchuan earthquake area. *Quat. Int.* 250, 63–73. <https://doi.org/10.1016/j.quaint.2010.11.020>.
- Yin, Y., Zheng, W., Liu, Y., Zhang, J., Li, X., 2010. Integration of GPS with InSAR to monitoring of the Jiayu landslide in Sichuan, China. *Landslides* 7, 359–365. <https://doi.org/10.1007/s10346-010-0225-9>.
- Zebker, H.A., Villasenor, J., 1992. Decorrelation in interferometric radar echoes. *IEEE Trans. Geosci. Remote Sens.* 30, 950–959. <https://doi.org/10.1109/36.175330>.
- Zhang, L., Lu, Z., Ding, X., Jung, H.-s., Feng, G., Lee, C.-W., 2012. Mapping ground surface deformation using temporarily coherent point SAR interferometry: application to Los Angeles basin. *Remote Sens. Environ.* 117, 429–439. <https://doi.org/10.1016/j.rse.2011.10.020>.
- Zhao, C., Kang, Y., Zhang, Q., Lu, Z., Li, B., 2018. Landslide identification and monitoring along the Jinsha river catchment (Wudongde reservoir area), China, using the InSAR method. *Remote Sens.* 10, 993. <https://doi.org/10.3390/rs10070993>.
- Zhou, X.P., Liu, J., Xu, C., 2020. A modified inverse-velocity method for predicting the failure time of landslides. *Eng. Geol.* 268, 105521. <https://doi.org/10.1016/j.enggeo.2020.105521>.